Supporting Information

Carrier Dynamics and Interactions for Bulk-like Photoexcitation of Colloidal Indium Arsenide Quantum Dots

Austin P. Spencer[†‡] William K. Peters[†§] Nathan R. Neale[¶]
David M. Jonas[†]

† Department of Chemistry, University of Colorado, Boulder, CO 80309-0215, USA

‡ Current address: Department of Chemistry, Northwestern University, Evanston, IL 60208, USA

§ Current address: Los Alamos National Laboratory, Los Alamos, NM 87545, USA

¶ Chemistry and Nanoscience Center, National Renewable Energy Laboratory, 15013 Denver West Parkway, Golden, CO 80401, USA

Contents

1 Materials

Tris(trimethylsilyl)arsine ($As[Si(CH_3)_3]_3$) was isolated as a viscous, colorless liquid by vacuum distillation (48°C, 10 mTorr) from the salt metathesis between sodium-potassium arsenide—prepared via reduction of As^0 (powder, ≥99.997% trace metals basis, Sigma-Aldrich) with NaK alloy—and trimethylsilylchloride (distilled over CaH_2 under nitrogen atmosphere) in dimethoxyethane (dried over Na^0/benzophenone ketyl, distilled under nitrogen atmosphere) according to the published procedure.[1] Indium(III) chloride (anhydrous, powder, ≥99.999% trace metals basis, Signma-Aldrich) was used as-received. Trioctylphosphine (TOP, technical grade, 90%, Sigma-Aldrich) was dried at 10^{-2} Torr at 100°C for at least 12 h, and triocytylphosphine oxide (TOPO, ReagentPlus, 99%, Sigma-Aldrich) was dried at 10^{-2} Torr over P_2O_5 for at least 12 h. Toluene and methanol were dried over Na^0 and distilled under nitrogen atmosphere. All solutions were handled in a nitrogen-filled glove box, and nanocrystal synthesis was performed on a Schlenk line using standard techniques.

2 Indium Arsenide Quantum Dots (InAs QDs)

InAs QDs were prepared by adaptation of literature procedures of Peng and Alivisatos,[2] Cao and Banin,[3] and Yu and Nozik.[4] As in ref. 4, TOPO was added to stabilize the surface without a shell. A 1:2.5 (w/w) solution of $InCl_3$ and TOP was prepared by vigorous stirring overnight. This viscous, pale-yellow solution was mixed with $As[Si(CH_3)_3]_3$ and TOPO to obtain a deep orange solution. Full weights and molar ratios are provided in Table S1. The reaction vessel was a 50-mL, 3-neck (14/20 joints) quartz round-bottom flask attached to a reflux condenser fitted with a flow-control adaptor attached to the Schlenk line via hose. The round-bottom flask contained 2.0 mL of TOP initially was heated to 300°C, and the orange stock solution was injected according to the sequence detailed in Table S2. Following the initial nucleation at 300°C, growth at 260°C was conducted by subsequent injections (temperature monitored by a thermocouple inserted into the reaction mixture through a septum). The stock solution volume was increased slightly with each subsequent injection to account for the increasing QD diameter.

In the glove box, toluene (10 mL) was added, and the crude mixture was stirred vigorously before allowing to settle. The dark brown-black solution was separated from the solids via pipet, and the solids were washed with additional toluene (5 mL). InAs QDs were purified and size-selected using toluene and methanol. First, methanol (20 mL) was added to the combined toluene extracts (totaling ∼25 mL) and the resulting precipitate separated by centrifugation at $12,000 \times g$. The brown, transparent solution was decanted, leaving a biphasic black solid and oil. A second purification of the solid/oil mixture using the same toluene (10 mL) followed by methanol (2.5 mL) solvent/antisolvent technique produced an oily black solid, which was dissolved in toluene (25 mL) followed by methanol (10 mL) and centrifuged a third time. The black solid (no longer oily)

Table S1: InAs QD stock solution composition.

	$InCl_3$	$As[Si(CH_3)_3]_3$	TOP*	TOPO
MW (g/mol)	221.18	294.95	370.64	386.64
Wt (g)	1.81	1.65	4.53	0.016
mmol	8.18	5.58	12.2	0.041
Molar Ratio	1.47	1.00	2.19	0.007

*Does not include 2.0 mL in 50-mL round-bottom flask.

Table S2: InAs QD stock solution injection sequence into 2.0 mL TOP.

Injection	Stock Solution Volume (mL)	Time (min)	Temperature (°C)
#1	1.00	0	300
#2	0.65	20	260
#3	0.65	50	260
#4	0.65	60	260
#5	0.70	70	260
#6	0.75	80	260
#7	0.85	90	260
#8	0.95	100	260
#9	1.00	110	260
Cool Down*	-	130	-

*Cooling to ambient temperature was accomplished in ∼5 min by removing the heating mantle.

was purified one additional time using toluene (10 mL) and methanol (30 mL) followed by centrifugation and decanting the light brown supernatant. Analysis of the weakly colored supernatants showed that these contained smaller diameter particles, as expected from size-selective precipitation. The obtained black solid product was soluble in toluene but not hexanes, indicative of minimal excess ligand. Given the absence of competitive ligands with strong affinities for metal atoms (e.g., the phosphonate or carboxylate ligands in ref. 5), it is plausible that the TOPO ligands remain bound to the In atoms on the InAs QD surface after the 4-step size-selective precipitation with methanol and toluene in the synthesis described here, though it is likely that complete surface passivation is not achieved.

3 Transmission electron microscopy images

Transmission electron microscopy (TEM) images (Figure S1) suggest that the QDs are roughly spherical. Although they do have some polygonal features, QDs do not appearing to be elongated in any dimension. An analysis of 110 QDs using a spherical shape model indicated a mean (median) QD diameter of

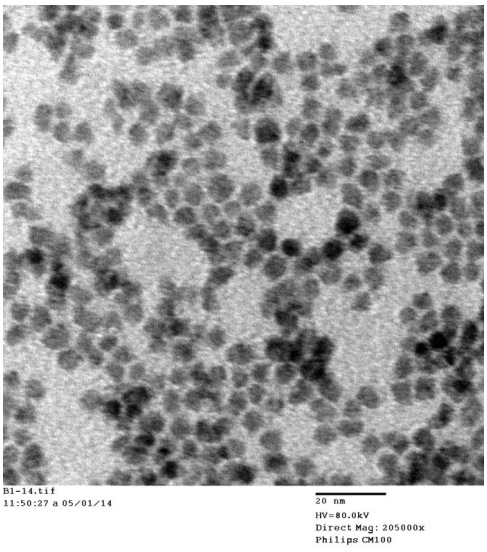

Figure S1: Transmission electron micrograph of the colloidal InAs QD sample. Fitting individual QDs to a spherical shape model yields median and mean QD diameters of 6.18 nm and 6.21 nm, respectively, with a standard deviation of 0.72 nm. The image has a magnification factor of 205,000. A 20 nm scale bar is shown beneath.

6.18 nm (6.21 nm) with a standard deviation of 0.72 nm.

4 Focal spot size

The focal spot of pump and probe beams at their crossing point in the sample location was characterized using an imaging sensor (ZoomCam USB Model 1598 with lens removed; 330K pixel CMOS sensor; 7.4 μm pixel size; 8-bit depth), yielding an intensity FWHM beam focal spot size of 48 μm.

5 Linearity of absorption

Linearity of pump pulse transmission was tested by measuring the pump pulse energy before and after transmission through the InAs sample as compared to a solvent (toluene) blank. A saturation fit (see "Saturation Model" section in main text) to the transmitted pump pulse energy in Figure S2 suggests that nonlinear contributions to pump pulse absorption are below the 0.2% level for probe-weighted spatially-averaged excitation probabilities up to 1.2.

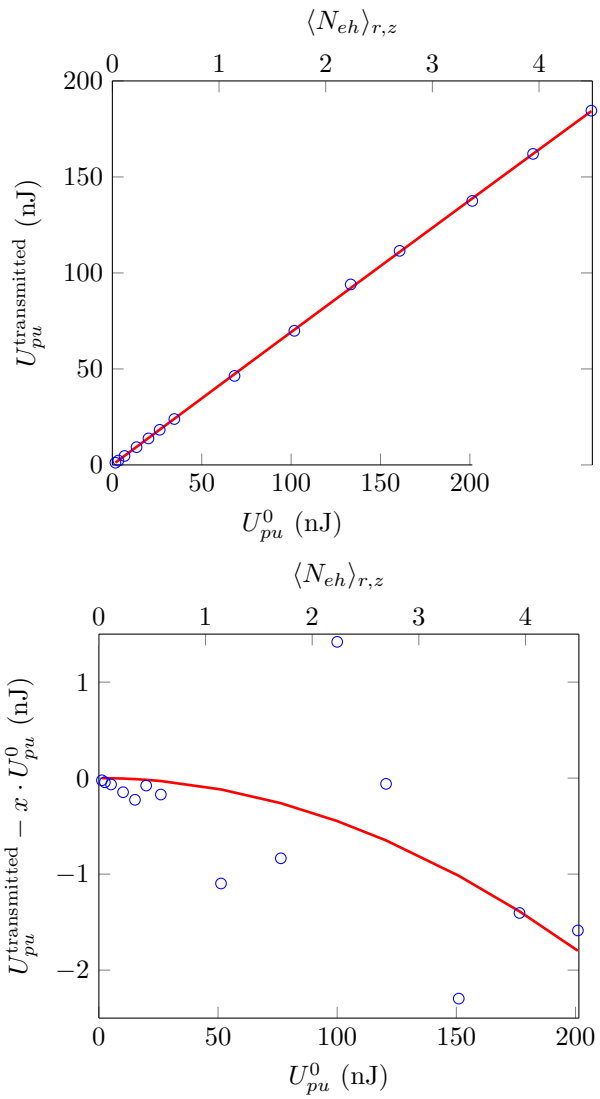

Figure S2: Transmitted pump pulse energy, $U_{pu}^{\text{transmitted}}$, as a function of incident pump pulse energy, U_{pu}^{0}, (blue circles) for the InAs QD sample and a saturation model fit (red line) with $x = 0.926$ and $y = 4.85 \cdot 10^{-5}$. In the lower panel, the linear component of the saturation fit has been subtracted from both the saturation fit (red line) and transmitted pump pulse energy (blue circles). Sample path length, $L = 250$ µm; optical density, OD($\lambda = 793$ nm) $= 0.04$; laser repetition rate, $k_{\text{laser}} = 20$ kHz; beam spot size, $w = 127$ µm.

6 Model of repetitive excitation

The effect of repetitively exciting the sample was evaluated by measuring the pump power dependence of pump–probe signal at $T = 1$ ns with beam scanning pattern durations of $\tau_{\text{pattern}} = 38.6$ ms and $\tau_{\text{pattern}} = 614$ ms, as illustrated in Figure S3. No difference is observed between the two tested pattern durations within the signal-to-noise of the measurement. Assuming that upon excitation by the pump pulse, the quantum yield for entering a long-lived state with lifetime τ_{LLS} is ϕ_{LLS} and that excitons in long-lived states do not contribute to pump–probe signal, an upper limit for the quantum yield–lifetime product can be estimated. The steady-state buildup of a trap state population evaluated using a two-state model that includes a ground state (GS) and a trap state (TS)

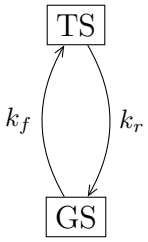

where the rates for entering and leaving the trap are $k_f = \phi_{LLS}\langle N_{eh}\rangle_{r,z} k_{\text{resampling}}$ and $k_r = 1/\tau_{LLS}$, respectively. If the ground state and trap state probabilities sum to 1, then the steady-state probability of the trap state is

$$\begin{aligned}[TS] &= \frac{k_f}{k_f + k_r} \\ &= \frac{\phi_{LLS}\langle N_{eh}\rangle_{r,z} k_{\text{resampling}}}{k_r + \phi_{LLS}\langle N_{eh}\rangle_{r,z} k_{\text{resampling}}}.\end{aligned} \tag{S1}$$

Solving for ϕ_{LLS}/k_r yields

$$\frac{\phi_{LLS}}{k_r} = \phi_{LLS} \cdot \tau_{LLS} = \frac{[TS]}{1 - [TS]} \frac{1}{\langle N_{eh}\rangle_{r,z} k_{\text{resampling}}}. \tag{S2}$$

At the highest probe-weighted spatially-averaged excitation probability in Figure S3 ($\langle N_{eh}\rangle_{r,z} = 2.72$), the combined uncertainty in the data between the two pattern durations ($2.43 \cdot 10^{-5}$) is 11.3% of the signal size ($2.15 \cdot 10^{-4}$). Therefore, if the trap state yields no pump–probe signal at 1 ns delay (as also expected for an initially charged QD because of the fast trion decay), the trap state could account for as much as 11.3% of the QD population at the highest excitation probability. An upper bound on $\phi_{LLS} \cdot \tau_{LLS}$ is thus calculated from eq. S2 by substituting $\tau_{\text{pattern}} = 38.6$ ms, $\langle N_{eh}\rangle_{r,z} = 2.72$, and $[TS] = 0.113$ on the right-hand side to yield $\phi_{LLS} \cdot \tau_{LLS} \leq 0.00181$ s. This upper bound on $\phi_{LLS} \cdot \tau_{LLS}$ indicates that the percentage of QD population in the trap state is less than 0.03% for $\langle N_{eh}\rangle_{r,z} = 9.0\%$ and $\tau_{\text{pattern}} = 614$ ms. Even at an excitation probability of 200%, eq. S1 above predicts that the steady-state accumulation of trapped or photocharged products should be below 2.5% at a resampling rate of 6.3 s^{-1}.

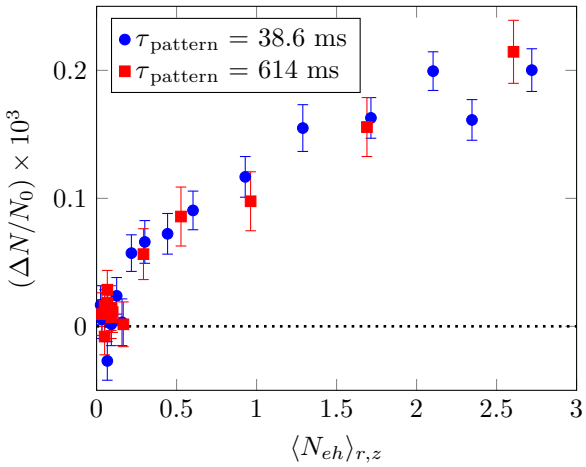

Figure S3: Pump–probe signal, $\Delta N/N_0$, measured as a function of probe-weighted spatially-averaged excitation probability, $\langle N_{eh} \rangle_{r,z}$, with beam scanning patterns of time duration $\tau_{\text{pattern}} = 38.6$ ms (blue circles) and $\tau_{\text{pattern}} = 614$ ms (red squares). Sample path length, $L = 1$ mm; optical density, OD($\lambda = 793$ nm) $= 0.1$; laser repetition rate, $k_{\text{laser}} = 10$ kHz; beam spot size, $w = 64$ µm.

7 Saturation model

The ability of the saturation model to capture the scaling of $1 - \langle P_0 \rangle_{r,z}$ is exhibited in Figure S4. The saturation fit to $1 - \langle P_0 \rangle_{r,z}$ at low $\langle N_{eh} \rangle_{r,z}$ (green dotted line in Figure S4) demonstrates that the saturation model captures the functional form of $1 - \langle P_0 \rangle_{r,z}$ as $\langle N_{eh} \rangle_{r,z}$ increases up to ∼0.6.

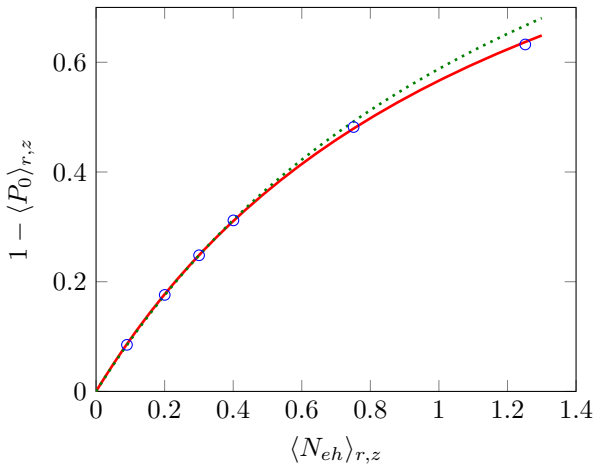

Figure S4: Saturation fit (red line) to $1 - \langle P_0 \rangle_{r,z}$, the probe-weighted spatially-averaged excitation probability of a QD being excited at least once (blue circles), yielding saturation parameters $x = 1.03$ and $y = 0.819$. A saturation fit including only $\langle N_{eh} \rangle_{r,z} \leq 0.25$ (green dotted line) gives $x = 1.00$ and $y = 0.700$ and exposes subtle functional differences between the saturation model and $1 - \langle P_0 \rangle_{r,z}$ that start to become experimentally significant for $\langle N_{eh} \rangle_{r,z} > 0.6$. Sample path length, $L = 1$ mm; optical density, OD($\lambda = 793$ nm) $= 0.1$; beam spot size, $w = 41$ µm.

8 Saturation model fits

The parameters $x(T)$ and $y(T)$ from a saturation fit to six experimental pump–probe transients with a range of probe-weighted spatially-averaged excitation probabilities are shown in Figures S5 and S6. $x(T)$ is proportional to the linear signal reconstruction, eq. 8, and contains single exciton dynamics. $y(T)$ is proportional to the level of signal saturation at a given pump–probe delay and therefore rises on the timescale of AR and asymptotically approaches a constant value at long pump–probe delays once AR is complete.

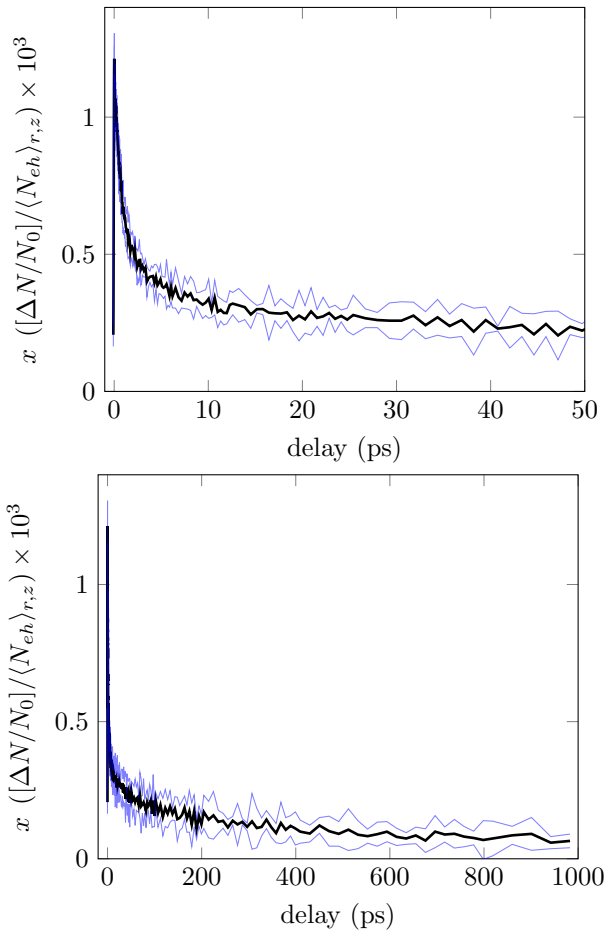

Figure S5: Saturation model parameter x (black line) as a function of pump–probe delay T and 95% confidence intervals (blue lines). x is the result of independent saturation fits at each T to the set of six transients with probe-weighted spatially-averaged excitation probabilities given in Table 1. Sample path length, $L = 1$ mm; optical density, OD($\lambda = 793$ nm) $= 0.1$; laser repetition rate, $k_{\text{laser}} = 10$ kHz; beam spot size, $w = 41$ µm; average resampling time, $\langle \tau^{\text{resampling}} \rangle = 0.33$ s.

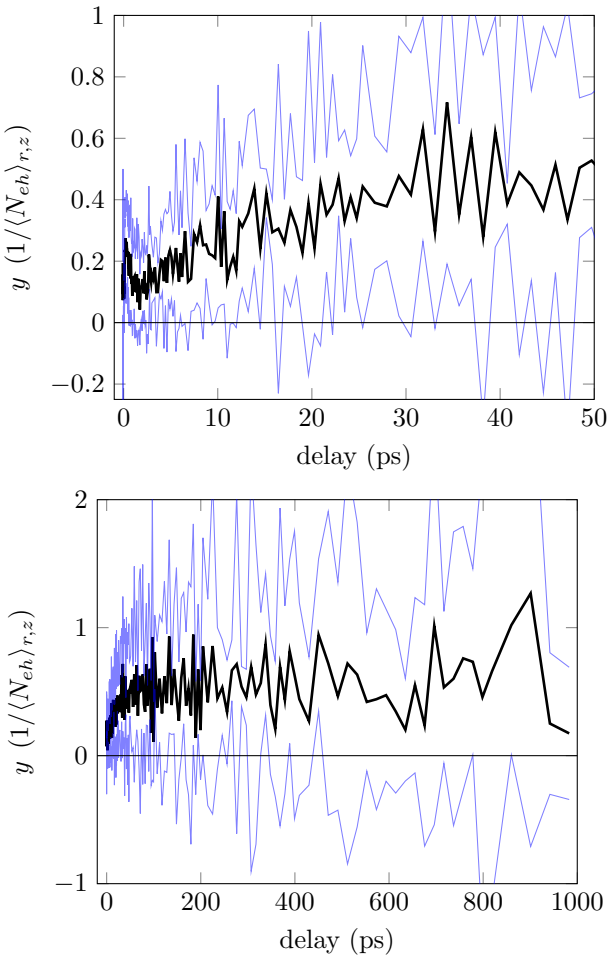

Figure S6: Saturation model parameter y (black line) as a function of pump–probe delay T and 95% confidence intervals (blue lines). y is the result of independent saturation fits at each T to the set of six transients with probe-weighted spatially-averaged excitation probabilities given in Table 1. Sample path length, $L = 1$ mm; optical density, OD($\lambda = 793$ nm) $= 0.1$; laser repetition rate, $k_{\text{laser}} = 10$ kHz; beam spot size, $w = 41$ µm; average resampling time, $\langle \tau^{\text{resampling}} \rangle = 0.33$ s.

References

[1] Becker, G.; Gutekunst, G.; Wessely, H. J. Trimethylsilylverbindungen Der Vb-Elemente. I Synthese Und Eigenschaften Von Trimethylsilylarsanen. *Z. Anorg. Allg. Chem.* **1980**, *462*, 113–129.

[2] Peng, X.; Wickham, J.; Alivisatos, A. P. Kinetics of II-VI and III-V Colloidal Semiconductor Nanocrystal Growth: "Focusing" of Size Distributions. *J. Am. Chem. Soc.* **1998**, *120*, 5343–5344.

[3] Cao, Y. W.; Banin, U. Growth and Properties of Semiconductor Core/Shell Nanocrystals With InAs Cores. *J. Am. Chem. Soc.* **2000**, *122*, 9692–9702.

[4] Yu, P.; Beard, M. C.; Ellingson, R. J.; Ferrere, S.; Curtis, C.; Drexler, J.; Luiszer, F.; Nozik, A. J. Absorption Cross-Section and Related Optical Properties of Colloidal InAs Quantum Dots. *J. Phys. Chem. B* **2005**, *109*, 7084–7087.

[5] Zeng, B.; Palui, G.; Zhang, C.; Zhan, N.; Wang, W.; Ji, X.; Chen, B.; Mattoussi, H. Characterization of the Ligand Capping of Hydrophobic CdSe–ZnS Quantum Dots Using NMR Spectroscopy. *Chem. Mater.* **2018**, *30*, 225–238.